The lipid-mediated mechanism of mechanosensitive channel MscS inactivation

Elissa Moller [1,2,3], Madolyn Britt [1,2], Fei Zhou [1], Hyojik Yang [4], Andriy Anishkin [2], Robert Ernst [4], Juan M. Vanegas [5], Sergei Sukharev [2,3,#], Doreen Matthies [1,#]

[1] Unit on Structural Biology, Division of Basic and Translational Biophysics, *Eunice Kennedy Shriver* National Institute of Child Health and Human Development, National Institutes of Health, 29 Lincoln Dr, Bethesda, MD 20982, USA.

[2] Department of Biology, University of Maryland, College Park, MD, 20742, USA.

[3] Institute for Physical Science and Technology, University of Maryland, College Park, MD, USA.

[4] Department of Microbial Pathogenesis, University of Maryland School of Dentistry, Baltimore, MD, 21201, USA.

[5] Department of Biochemistry & Biophysics, Oregon State University, Corvallis, OR, 97331, USA.

Correspondence to Sergei Sukharev (sukharev@umd.edu) and Doreen Matthies (Doreen.Matthies@nih.gov)

Keywords: native nanodiscs, cryo-EM, mechanosensation, membrane protein structure, polymer extraction, protein-lipid interaction

Abbreviations: mechanosensitive channel of small conductance (MscS), transmembrane (TM), Electron Microscopy (EM), Blue Native (BN), Mass Spectrometry (MS), Molecular Dynamics (MD), phosphatidylethanolamine (POPE), phosphatidylglycerol (POPG), cardiolipin (CL)

Abstract

Interpretations of experimental conformations of mechanosensitive channels gated by 'force from lipids' become more reliable when native lipids are preserved in the structures. *Escherichia coli* MscS is an adaptive osmolyte release valve that regulates turgor in osmotically stressed cells. MscS promptly opens under abrupt super-threshold tensions in the membrane, but at lower and more gradually applied tensions, it silently inactivates from the closed state. A central question has been whether to assign the commonly observed non-conductive conformation with splayed peripheral helices to a closed or inactivated state. We present a 3-Å MscS cryo-EM structure obtained in Glyco-DIBMA polymers, which avoid complete lipid removal. Within the complex, we observe densities for endogenous phospholipids intercalating between the peripheral and pore-lining helices. The lipidomic analysis shows a 2-3 fold enrichment of phosphatidylglycerol in Glyco-DIBMA-extracted MscS samples. The computed pressure of these lipids on the protein surface enforces the characteristic kinks in the pore-lining helices, sterically stabilizing the separation of the peripheral helices. Mutations of residues coordinating lipids in the crevices eliminate inactivation, allowing us to classify this group of structures as the inactivated state. Our study reveals a novel inactivation mechanism in which intercalated lipids physically decouple the tension-sensing helices from the gate.

Introduction

MscS is a ubiquitous prokaryotic mechanosensitive channel of small conductance first identified in *Escherichia coli* [1] where it acts as an adaptive low-tension-threshold osmolyte release valve that regulates turgor pressure and ensures osmotic shock survival. It is the key cytoplasmic membrane component that provides bacterial adaptation to freshwater, which is the main transmission route for commensals and pathogens [2]. The unique structural design of MscS was evolutionarily preserved and diversified in several paralogs present in the genomes of free-living bacteria [1,3]. Multiple MscS homologs are found in all clades of walled organisms, including archaea, protists, fungi, and plants [4-6]. In eukaryotes, MscS homologs fulfill sensory functions [7,8] and impart osmotic stability to internal organelles [9,10]. The MscS structure's manifestation in multimodal adaptive behavior warrants detailed analysis.

E. coli MscS is a homo-heptamer with each 287-residue protomer comprising three transmembrane helices and forming a large hollow cytoplasmic domain as revealed by the first crystal structure (PDB 2OAU [11,12]). MscS is gated directly by tension transmitted through the surrounding lipid bilayer [13,14]. Patch-clamp experiments in spheroplasts show that MscS readily opens in response to abruptly applied super-threshold tension but gradually inactivates under prolonged application of near-threshold tension. Its functional cycle comprises three functional states and two alternative transitions: closed-to-open and closed-to-inactivated, the latter state being non-conductive and tension-insensitive [15-17]. The opening-closing transitions are sharply tension-dependent, essentially non-dissipative, and can be very fast [17-20]. In contrast, the inactivation and recovery transitions are slow [16,17] but can be modulated by depolarizing voltages [19] and crowding pressure in the cytoplasm [21]. Analysis of mutations shows that the propensity toward inactivation depends on the flexibility of pore-lining helices [15], salt bridges between the TM and cytoplasmic domains [20], hydrophobicity of TM2-TM3 crevices [22], and the residues that anchor the protein to the inner leaflet [19]. While MscS opens robustly in most tested lipid environments [13,14,23,24], inactivation is not observed when MscS is reconstituted in soybean lipids [13,14], suggesting that lipids may be inseparable players in the mechanism of MscS inactivation and maintenance of the active state.

Although there are three functional states, only two classes of MscS structures exist. The first crystal structure of *E. coli* MscS, solved in Fos-choline-14 (PDB 2OAU [11,12]), is to the first from the class characterized by splayed peripheral helices. The TM1-TM2 helical pairs in these conformations are disconnected from the sharply kinked TM3s that form the transmembrane pore and the gate. The hydrophobic gate of the 2OAU structure was found de-solvated in MD simulations [25], and thus the splayed structure was deemed non-conductive. More recent cryo-EM structures solved in mixed micelles or lipid nanodiscs (PDBs 6UZH, 7ONL, 7OO6, 7OO8, 6LRD, 6PWN, 6PWP, 6YVK [26-30]) are more

complete but generally retrace the original 2OAU [11,12] conformation. The second type of MscS conformation was observed in the A106V mutant (PDB 2VV5 [31]), adopting an expanded barrel structure. This conformation was classified as open. However, estimations suggest that this conformation only achieves half of the experimental conductance of the fully open MscS (See Extended Data Fig. 1 and Text). Soon after, a similar expanded structure of WT MscS was solved in detergent DDM [32] and more recently in nanodiscs formed of short-tail lipids [28,33]. These semi-open conformations have never been observed in the presence of lipids with regular full-length tails. The semi-open conformation of WT MscS, which is stable in a pure detergent environment (2VV5 class), can be converted into a splayed non-conductive state (2OAU class) simply by adding a low mole fraction of regular phospholipids [26]. Notably, the two observed classes of conformations do not explain the entire three-state functional cycle of MscS.

Non-conductive splayed conformations of MscS have highly developed lipid-facing surfaces with characteristic crevices. Higher resolution structures detected densities of lipids stably associated with the splayed non-conductive structure of MscS, with one lipid consistently found closer to the periplasmic surface and more lipids on the cytoplasmic side [26-29]. Simulations have shown that the splayed non-conductive structures specifically produce substantial distortion of the lipid bilayer on the cytoplasmic side, pulling the lipids into the crevices below the bilayer boundary and orienting them parallel to the bilayer plane [33,34]. In addition, the fluorescence of tryptophan substitutions in the crevices detected an exchange of brominated lipids between these regions and the bulk bilayer [34]. The splayed lipid-filled structure was interpreted as the closed state, and the hypothetical re-distribution of lipids between the crevices and the bilayer, driven by membrane tension, has been proposed as the opening mechanism [35]. A subsequent finding of single-tail lipid-like densities inside the pore of MscS reconstituted into nanodiscs prompted an even more elaborate model of MscS gating by the 'hook lipid' and single-tail lipids traveling in and out of the pore [27].

Presenting the MscS gating cycle as two states (closed ↔ open) [27,33,35] is a simplification that neglects the second non-conductive functional state of MscS, the prominent inactivated state [16,17], which holds clear biological importance [36,37]. To address this gap, we determined the structure of MscS extracted by the novel Glyco-DIBMA polymer [38], which preserves the positions of native lipids associated with the complex. During a typical membrane protein purification, lipids are largely removed by detergents prior to structural determination (Extended Data Fig. 2b). Detergents mimic the lipid bilayer environment to some extent but can cause structural changes [39]. After solubilization, exogenous lipids are typically reintroduced in the form of mixed micelles, liposomes, or synthetic nanodiscs (Extended Data Fig. 2c-e) [39]. However, extraction from the native membrane with detergent is still a prerequisite step. A more recent

119 approach is to use amphipathic polymers to extract membrane proteins directly out of the lipid bilayer
120 (Extended Data Fig. 2f), avoiding a complete de-lipidation step [40]. Retaining a part of the local lipid
121 environment provides the necessary detail on what lipids copurify and in what specific positions they
122 associate with the protein [41-46].
123
124 In this work, we resolve the MscS conformation to 3 Å with intercalated lipids in specific conformations
125 in the crevices and determine the key residues stabilizing their positions. We use Mass Spectrometry (MS)
126 to determine the lipid species that preferentially associate with the complex. Molecular Dynamics (MD)
127 simulations show the stable residence of these non-bilayer lipids that physically separate the lipid-facing
128 helices from the pore-lining helices that form the gate. Computations of local 3D pressure exerted by the
129 intercalating aliphatic tails reveal the pattern that stabilizes the characteristic kinked conformation of the
130 pore-forming helices. We then mutate the residues that coordinate the lipid headgroups and analyze the
131 mutant's functional behavior by patch-clamp electrophysiology. Our data indicate that the splayed
132 structure with intercalated lipids represents the inactivated state, which illustrates a novel lipid-mediated
133 inactivation mechanism that uncouples the tension-receiving peripheral helices from the gate.
134
135 **Results**
136 *Cryo-EM of MscS in native nanodiscs*
137 Out of the three polymers we attempted (see Extended Data), only Glyco-DIBMA [38], a novel polymer that
138 has not been used previously for cryo-EM, produced the whole *E. coli* MscS structure. Upon extraction
139 and cobalt affinity column purification, the identity of polymer-extracted MscS was confirmed by SDS-
140 PAGE and Western Blot (Extended Data Fig. 3d,g). Despite the high fraction of heavy particles inside
141 large membrane patches, we proceeded to cryo-EM based on the 2D class averages from negative staining
142 EM data collection (Extended Data Fig. 3m,p). The resulting map of MscS extracted with Glyco-DIBMA
143 reached an average resolution of 2.99 Å, with the cytoplasmic domain estimated at 2.6 Å (Fig. 1). The
144 structure is non-conductive, with the TM helices tilted inward at the top and splayed away from the pore-
145 lining helix. The 2D class averages that contributed to this 3D reconstruction comprised the isolated
146 particles associated with small lipid patches around the protein.
147
148 Densities unaccounted for by the protein model were examined for the presence of characteristic aliphatic
149 chains and modeled as four individual phospholipids designated as Lipids 1 to 4. Because the resolution
150 of dynamic lipids is insufficient to discern the headgroups, both POPE and POPG were possible
151 candidates. Guided by lipidomic MS data (below), we were able to infer the lipid species and simulate
152 their dynamic behavior. However, to avoid overinterpretation, in the final structure, the lipids are modeled

153 with the headgroup truncated after the phosphate. The aliphatic tails of Lipid 1 (Fig. 2a) are oriented
154 along TM1 and TM2 helices of neighboring chains, with the phosphate group latching to R88, forming a
155 characteristic 'hook' [27]. Lipids 2-4 (Fig. 2b-d) are oriented with the tails parallel to the inner surface of the
156 membrane bilayer, wedged between the TM1-2 helices of neighboring chains. The protein-lipid contacts
157 are stabilized by the electrostatic interactions between the lipid headgroups and charged residues in the
158 gaps and crevices, most noticeably R88 for Lipid 1 and R59, K60, and D67 for Lipids 2-4. Multiple
159 nonpolar contacts between hydrophobic residues and the aliphatic chains also occur. A full list of nearby
160 residues stabilizing lipids in the static cryo-EM density-based structure is given in Extended Data Table 1.
161 The extraction by the Glyco-DIBMA polymer [38] produced lipid patches of various sizes around the
162 protein. The electron density surrounding the small native nanodisc patches from which we could resolve
163 the structure is tighter than is typically seen in a pure detergent micelle. This polymer coat, along with the
164 other remaining unmodeled densities that were not clearly defined lipids or proteins, is shown in
165 Extended Data Fig. 4a,b. As was reported previously for detergent-extracted MscS reconstituted in
166 synthetic lipid nanodiscs [27], we also observe several lipid-like densities inside the hydrophobic section of
167 the channel pore. These particles do not have densities that could represent a phospholipid headgroup and
168 appear to represent single aliphatic chains. As will be discussed below, these are possible *E. coli* fatty acid
169 metabolites that are produced in the cytoplasm [47] and quickly exported to the periplasm [48].
170
171 *Mass Spectrometry of MscS-copurified lipids*
172 MALDI-QTOF MS analysis was conducted on lipids copurified with MscS during extraction with Glyco-
173 DIBMA and enrichment on a cobalt affinity column. The affinity-purified particles were subjected to an
174 additional step of gel-filtration chromatography to isolate the smallest particles containing primarily
175 annular lipids closely associated with the protein (Extended Data Fig. 4f). Fig. 2f and Extended Data
176 Table 2 provide a comparison of the lipids co-purified with MscS with the composition of the inner
177 membrane fraction isolated from the same expresser strain using a sucrose gradient. Using the Fast Lipid
178 Analysis Technique (FLAT) -MS method for the characterization of lipid A and phospholipids [49], two
179 highly abundant POPE species with one unsaturated bond, two prevalent POPG species, and two
180 cardiolipin (CL) species were identified (Extended Data Fig. 4g). The *E. coli*-specific lipid A shows its
181 typical m/z of 1796.21. A table comparing the relative amounts of lipids between the two samples, inner
182 membrane (M) and protein (S), shows that odd chain POPE 33:1 and the two POPGs are enriched
183 approximately 2-fold, other lipids POPE 32:1, Cardiolipins, are slightly enriched, whereas lipid A is
184 largely excluded from the protein-associated pool (Fig. 2f).
185
186 *Lipid coordination and dynamics in the crevices*

To better understand the dynamics of protein-lipid interactions, we embedded the solved structure with lipids in a POPE/POPG (3:1) lipid bilayer, equilibrated the system with soft restraints on the protein backbone for 20 ns, and ran for 100 ns in unrestrained simulations. Based on the lipid enrichment seen in MS, we embedded POPG as Lipids 1-3 and POPE as Lipid 4. The representative snapshots of lipid conformations in interhelical crevices are shown in Fig. 3, where Lipids 1-4 are color-coded individually. While the overall positions of lipids remained stable, they engaged with a broader set of surrounding polar sidechains compared to the static cryo-EM structure. In these simulations, Lipid 1 maintains a stable contact with R88 at the periplasmic side of MscS, and it is the only membrane lipid that contacts this residue. The average total probability of the headgroup contact is about 1.5 per subunit, half of which engage with the fatty acid oxygens of Lipid 1, and the other half with the phosphate group. Lipids 2, 3, and 4 interact primarily with the residues R59 and D67 located at the cytoplasmic side. Fig. 3b-d show that the aliphatic chains of the intercalated lipids frequently go around the TM2 helix and thus physically separate it from the TM3s forming the hydrophobic gate (L105-L109). Besides that, these lipids form electrostatic contacts with R74. The contact probabilities were scored for each individual lipid, emphasizing electrostatic interactions of phosphate and fatty acid oxygens or amino groups with neighboring sidechains. The statistics of polar contacts within 5 Å of each specific group averaged over all subunits during the last 80 ns period of the simulation are shown in Extended Data Table 3. Fig. 3c-d show the multiplicity of H-bonding patterns between the headgroups within the three-lipid cluster, illustrating the low entropic restraint allowing for a stable residence of three lipids in the crevice in multiple configurations.

Fig. 4 shows the local stress distribution on the surface of individual MscS chains through the traction vector. The 3D local stress was computed from a parallel simulation of the solved MscS structure in GROMACS and analyzed with the GROMACS-LS package (see Methods). The normal component of the traction shows various ‘hot spots’ of pushing (blue) and pulling (red) forces on the surface of the channel subunits (Fig. 4b), which incorporates interactions with the surrounding lipids and solvent molecules. The enlarged region near the partially de-solvated portion of the pore (Fig. 4c) shows pulling forces, while prominent pushing forces exerted by lipid chains are concentrated precisely in the kinked region of TM3 near L111 and G113. The pressure of intercalated lipids, therefore, stabilizes the G113 kink previously associated with the inactivated state [15].

Functional effects of crevice mutations

To investigate how protein interactions with the intercalating lipids affect the function of MscS, we conducted functional tests of several mutants using patch-clamp (Fig. 5). The 'hook' Lipid 1 is observed in

221 many structures [26-29]. It was predicted to play a role in the gating transitions by detaching and moving to
222 the bilayer during the opening transition [27]. Fig. 5a-b shows patch-clamp traces comparing WT MscS and
223 R88A, illustrating the depth of inactivation and the kinetics of recovery. The small hydrophobic
224 substitution R88A had a mild phenotype, with no significant changes to activating tension (Extended Data
225 Table 4) or percent inactivation but did show a subtle slowing down of the recovery from inactivation
226 (Extended Data Table 5). In our cryo-EM samples, the densities of aliphatic chains of Lipid 1 are clear,
227 but the nature of the headgroup cannot be easily identified. The interactions of the guanidine group of
228 R88 with the phosphate would stabilize almost any type of lipid in this place.
229
230 The polar headgroups of Lipid 2 and Lipid 3 predominantly interact with R59's sidechain, perhaps with
231 additional contribution from K60. Lipid 4 intermittently interacts with the nearby D67. We conducted
232 recordings using the inactivation/recovery protocol after introducing point mutations at R59, D67, and
233 K60 (Fig. 5). All single substitutions for R59 resulted in a non-inactivating phenotype (Extended Data
234 Table 5). R59S has the least amount of inactivation at +30 mV pipette potential (Fig. 5d), the voltage at
235 which WT is more resistant to inactivation. The traces show no sign of recovery, suggesting that this
236 mutant greatly resists inactivation under these conditions. Conversely, D67A inactivates completely,
237 recovers very quickly when the pipette pressure drops to zero (Fig. 5c), and causes a slight increase in
238 activation midpoint (Extended Data Table 4). Substitutions at K60 have an intermediate phenotype, with
239 slightly more inactivation and a slower rate of recovery (Extended Data Table 5). Double R59S/K60S and
240 triple R59S/K60S/D67A are both strongly non-inactivating (Fig. 5e,f). Based on these results, we
241 conclude that the lipid intercalated state of the TM2-TM3 crevice, stabilized primarily by R59 interacting
242 with the lipid phosphates and D67 interacting with the amino groups of POPE, corresponds to the
243 inactivated state of the channel. The lipid penetration is 'invited' by R59, and when the lipids get into the
244 crevice, they are additionally stabilized by D67. It is important to note that in the D67A mutant, R59 is in
245 place and electrostatically unopposed due to the absence of the nearby D67 chain. Therefore, D67A is
246 more willing to inactivate, but the lack of a counterpart for interaction with the amino group of POPE
247 (Lipid 4) may make POPE leave the crevice more quickly, and so the recovery is quick. The lipid
248 expulsion from the crevices might be cooperative, which is why the departure of Lipid 4 may promote the
249 exit of other lipids, resulting in the compaction of the transmembrane domain and the re-establishment of
250 the functionally predicted TM2-TM3 contact [22].
251
252 *Comparison of structures and lipid positions*
253 The backbone of the Glyco-DIBMA polymer-extracted MscS is most similar to PDB 6PWN [27] solved in
254 synthetic nanodiscs, and shares the same architecture as the 2OAU-class with the TM1-2 helices splayed

away from the pore-lining helix (Extended Data Fig. 5a). The lipid-coordinating side chains are clearly resolved, and the modeled lipid positions are the most similar to PDB 6LRD [29] (Extended Data Fig. 5h-j), but unlike those exogenously added synthetic lipids, endogenous *E. coli* inner membrane lipids are retained here. In semi-open DDM and LMNG solubilized structures, detergent molecules replace these lipids on the periphery of the protein (PDBs 7OO0, 7ONJ [26]). Without this de-lipidation caused by detergent, a new lipid (Lipid 2) was also resolved.

PDB 6PWN [27] has additionally modeled 7 single lipid tails without density for lipid headgroups in the pore of the protein above the gate oriented along TM3a. We also see disordered density in these regions but did not model them as lipids as they are along the symmetry axis of the protein and lack clear densities for headgroups (Extended Data Fig. 4a,b). Detergents have been modeled in these locations previously [26], but since we never used detergent in our preparation, our densities likely correspond to free fatty acids which are necessary intermediates in phospholipid metabolism [47,50]. The Glyco-DIBMA polymer could have 'mobilized' fatty acids during the extraction and let them penetrate the pore. Moreover, these free fatty acids are actively extruded to the extracellular space [48]. MS shows a number of molecular species smaller than phospholipids co-purified with the protein sample (See Extended Data Fig. 4g), but at this point, we cannot identify these species unequivocally. Based on the essentially frictionless opening process [51] and the microsecond kinetics of MscS closing [19], we have no reason to connect the presence of these particles in the pore with the gating process. More likely, the gating transitions reflect tension-dependent wetting and de-wetting of the hydrophobic gate [25].

Discussion

The results presented above answer the central question: Does the splayed non-conductive conformation represent the closed or inactivated state? We provide evidence that MscS harboring lipids between the splayed peripheral helical pairs is in the inactivated state. The solved structure had sufficient resolution to identify residues coordinating lipids between the helices (R59 and D67), and mutations of these residues destabilizing lipids in the crevices directly affected inactivation. The analysis of lipids tightly associated with Glyco-DIBMA extracted complexes showed some enrichment of anionic lipids, presumably residing in the crevices. The MD simulations of the solved structure illustrate how the aliphatic tails of lipids in the crevices penetrate between the TM2 and TM3 helices, separate the membrane-facing (TM1-TM2) helical pairs from the gate, and exert pressure that stabilizes the characteristic G113 kink in TM3, previously associated with the inactivated state [15]. The conclusion that the splayed state represents the inactivated state implies the existence of the alternative non-conductive conformation with TM1-TM2

288 pairs reconnected with the TM3 barrel (‘compact’ closed state) and is highly consistent with the three-
289 state ‘dashpot’ gating mechanism of MscS [16]. This conclusion fully corroborates the dramatic functional
290 effects of hydrophilic substitutions in the crevices, which lead to immediate tension-driven channel
291 inactivation without opening [22]. It also explains the nature of the two alternative conformational
292 pathways, fast opening and slow inactivation, both originating from the closed state [17-19].
293
294 The choice of the novel Glyco-DIBMA polymer [38] advanced our characterization of MscS, revealing the
295 positions of native lipids. Instead of complete de-lipidation, the polymer 'cuts' the protein out of its native
296 membrane together with associated lipids, which could be resolved in their native positions. In the course
297 of extraction and purification, no exogenous lipids were added, and detergents were never used. The
298 overall resolution of the protein was near 3 Å (Fig. 1), and the densities of four protein-intercalating lipids
299 (per subunit) were resolved (Fig. 2). The parallel MS analysis indicated POPG enrichment. The positions
300 and dynamics of POPG/POPE lipids in the crevices were tested in MD simulations of the solved
301 structure, which confirmed stable coordination of Lipid 1 by R88 and preferential coordination of the
302 cytoplasmic three-lipid clusters (Lipids 2-4) by R59 and D67. The lipid motions inside the cytoplasmic
303 side clusters were substantial as H-bonds interlinked the lipid headgroups in many different
304 configurations (Fig. 3), indicating minimal entropic penalty and favorably low energy.
305
306 Mutations of lipid-coordinating residues had different functional manifestations. R88 coordinating Lipid 1
307 was previously proposed to play a role in gating by liberating this hook lipid during the opening transition
308 [27]. Our patch-clamp results, in contrast, show that R88A substitution does not affect the opening,
309 inactivation, or recovery processes substantially (Fig. 5). However, the effects of uncharged substitutions
310 for R59 and D67 were more dramatic. The R59S mutant showed a vivid non-inactivating phenotype,
311 indicating that destabilization/depopulation of the cytoplasmic lipid cluster in the crevice prevents
312 inactivation. The single D67A substitution exhibited fast inactivation and fast recovery, suggesting that
313 R59 alone is able to stabilize lipids in the crevice and lead to inactivation, but in the absence of the second
314 ‘attachment point’ for the lipid cluster, the lipid exchange between the bilayer and the crevice becomes
315 faster. The triple R59S/K60S/D67A mutation that removes most of the polar attachment point for lipids
316 prevents inactivation. This result indicates that the lipid-intercalated structure represents not the closed
317 but the inactivated state. The functional behavior of these mutants alongside the lipid-filled structure
318 allows us to make this assignment for the entire class of ‘splayed’ structures.
319

Previous studies have already attempted to rationalize and interpret the initial crystal structure of MscS solved in a splayed conformation with sharply kinked TM3 helices (PDB 2OAU [11,12]). The hydrophobic gate in this structure is de-solvated, and the conformation must be non-conductive [25]. Soon after, our functional study of MscS revealed the presence of the prominent tension-insensitive inactivated state [16]. In patch-clamp, the channel population opened fully in response to an abrupt tension application, but only a fraction of channels responded to a slow tension ramp of the same amplitude, while the majority silently transitioned to the inactivated state. This behavior, which allows MscS to discriminate the stimuli according to their dynamics, was coined as the "dashpot" tension coupling mechanism. It was proposed that the splayed crystal structure must represent the inactivated state [16]. Indeed, the PDB 2OAU [11,12] conformation shows the peripheral lipid-facing helices (TM1-TM2) disconnected from TM3 that form the gate. The sharp kink at G113 orients the TM3b helix almost parallel to the membrane interface and prevents the splayed TM1-TM2 pairs from closing the gap and straightening along TM3s. The G113A mutation imposing higher helical propensity to the kink region was shown to suppress inactivation [15]. This result suggested that the G113 kink is not present in all conformations, and there must be a compact state with the TM3 gate region reconnected with peripheral helices through a predicted hydrophobic 'clutch' formed by the rings of conserved hydrophobic residues, F68 and L72 on TM2 and L111 and L115 on TM3 [22]. The "dashpot" was predicted to transmit the abruptly applied tension from TM2 to TM3 and open the gate. Under slowly applied tension, the "dashpot" was predicted to 'give up' and mechanically uncouple the peripheral helices from the gate. We now believe that the intercalating lipids resolved in the crevices act precisely as a viscous dashpot filler mediating a slow/delayed uncoupling. Moreover, our MD results show that the tails of crevice-intercalated lipids exert pressure on the G113 kink region (Fig. 4), thus stabilizing this kink that keeps the TM1-TM2 pairs separated from the gate.

What conformations may explain the three-state kinetic scheme with two independent opening and inactivation transitions? Fig. 6 shows the place of the solved structure in the three-state functional cycle of MscS. The structure represents a stable inactivated state. The expulsion of lipids from the crevices is predicted to compact the structure into a narrowly packed closed state. In this state, the peripheral (TM1-TM2) helical pairs form a hydrophobic contact with TM3s. At the same time, the characteristic kink at G113 relocates to conserved G121 to allow for compaction [15]. The reconnected TM3 and TM2 helices provide the transmission route for the tension received from the lipids by the peripheral TM1-TM2 pairs, producing the conformation that is now capable of opening by tension. From that state, the channel may undergo two alternative tension-driven transitions, opening or inactivation. The opening of MscS, a steeply tension-dependent process, is predicted to occur through tilting and complete straightening of pore-lining TM3 helices, which is accompanied by a 16-18 nm^2 in-plane protein expansion. Opening is

extremely fast and was shown to be essentially non-dissipative [51]. Inactivation is associated with a smaller effective expansion, and it is shown to be a much slower process dependent on the nature of lipid-anchoring residues [19]. This is highly consistent with the slow penetration of lipids into the crevice, thus literally implementing a 'dashpot' mechanism.

We could not find any evidence in the literature that the splayed conformation is definitively the closed state. Repeated attempts to open the splayed conformation in simulations were generally unsuccessful [33,34,52]. The presentation of MscS as a two-state (closed-open) system without inactivation found in these papers is an oversimplification that overlooks the third functional state. Not only is the inactivated state seen in patch-clamp traces, but its functional importance has also been demonstrated in osmotic viability experiments [36,37]. What is the functional role of the inactivated state? The integrity of the cytoplasmic membrane is critical for bacterial energetics [53,54]. Inactivation is a safeguard against spurious channel opening and leaky state of the membrane in actively metabolizing, hyperpolarized, and turgid cells. Transition into the inactivated state occurs when there is a need (1) to reduce the active population and limit the permeability response to low osmotic shocks to minimize metabolic losses, (2) to properly terminate the full permeability response to a strong down-shock involving both MscS and MscL [36,37] and (3) to eliminate metabolite leakage from a swollen cell when the peptidoglycan is compromised by either β-lactam antibiotics or lysozyme. The splayed lipid-stabilized inactivated state appears to be the most stable (default) state, preventing leakage. When the channel is isolated in the presence of regular lipids, this state is the only conformation that has been experimentally observed. The assignment of the splayed lipid-filled conformation to the inactivated state now puts all of the previous functional results and modeling predictions [15] into place: the G113 kink previously associated with the inactivated state to be stabilized by intercalating lipids; straightening this kink would allow the TM2 to reconnect with TM3 to form a hydrophobic 'clutch' for force transmission from the periphery to the gate [22].

In conclusion, this work shows that applied to the MscS channel, the 'force-from-lipids' gating mechanism is twofold: lipids at the protein boundary transmit external forces to the gating apparatus to open the channels, but at the same time, protein-penetrating lipids can interrupt the force transmission route and make the channel tension-insensitive. The presented findings give the first explanation of the extremely broad range of MscS's kinetic responses, from millisecond opening rates to tens of seconds for inactivation. The opening transition can be very fast and essentially frictionless, as it does not seem to involve deep penetration of lipids. The slow dynamics of lipid penetration into secluded locations in the protein, leading to inactivation, kinetically separates the two independent expansion pathways of opening and inactivation, which imitates a dashpot. The inactivated state is most stable, whereas the compact

388 closed conformation appears unstable in isolation, and the fully open state is transient and requires
389 tension. For these reasons, the closed and fully open states have not yet been visualized by structural
390 methods. Special means will be required to stabilize these conformations and solve them experimentally.

References

1 Levina, N. *et al.* Protection of *Escherichia coli* cells against extreme turgor by activation of MscS and MscL mechanosensitive channels: identification of genes required for MscS activity. *EMBO J.* **18**, 1730-1737 (1999).

2 Cabral, J. P. Water microbiology. Bacterial pathogens and water. *Int J Environ Res Public Health* **7**, 3657-3703 (2010). https://doi.org/10.3390/ijerph7103657

3 Edwards, M. D. *et al.* Characterization of three novel mechanosensitive channel activities in Escherichia coli. *Channels (Austin)* **6**, 272-281 (2012). https://doi.org/10.4161/chan.20998

4 Hamilton, E. S., Schlegel, A. M. & Haswell, E. S. United in diversity: mechanosensitive ion channels in plants. *Annu Rev Plant Biol* **66**, 113-137 (2015). https://doi.org/10.1146/annurev-arplant-043014-114700

5 Haswell, E. S., Phillips, R. & Rees, D. C. Mechanosensitive channels: what can they do and how do they do it? *Structure* **19**, 1356-1369 (2011). https://doi.org/10.1016/j.str.2011.09.005

6 Pivetti, C. D. *et al.* Two families of mechanosensitive channel proteins. *Microbiol.Mol.Biol.Rev.* **67**, 66-85, table (2003).

7 Hamilton, E. S. *et al.* Mechanosensitive channel MSL8 regulates osmotic forces during pollen hydration and germination. *Science* **350**, 438-441 (2015). https://doi.org/10.1126/science.aac6014

8 Jojoa-Cruz, S. *et al.* Structural insights into the Venus flytrap mechanosensitive ion channel Flycatcher1. *Nat Commun* **13**, 850 (2022). https://doi.org/10.1038/s41467-022-28511-5

9 Veley, K. M., Marshburn, S., Clure, C. E. & Haswell, E. S. Mechanosensitive channels protect plastids from hypoosmotic stress during normal plant growth. *Curr Biol* **22**, 408-413 (2012). https://doi.org/10.1016/j.cub.2012.01.027

10 Wilson, M. E., Jensen, G. S. & Haswell, E. S. Two mechanosensitive channel homologs influence division ring placement in Arabidopsis chloroplasts. *Plant Cell* **23**, 2939-2949 (2011). https://doi.org/10.1105/tpc.111.088112

11 Bass, R. B., Strop, P., Barclay, M. & Rees, D. C. Crystal structure of *Escherichia coli* MscS, a voltage-modulated and mechanosensitive channel. *Science* **298**, 1582-1587 (2002).

12 Steinbacher, S., Bass, R., Strop, P. & Rees, D. C. in *Current Topics in Membranes* Vol. 58 1-24 (Academic Press, 2007).

13 Sukharev, S. Purification of the Small Mechanosensitive Channel of Escherichia coli (MscS): the Subunit Structure, Conduction, and Gating Characteristics in Liposomes. *Biophysical Journal* **83**, 290-298 (2002). https://doi.org/https://doi.org/10.1016/S0006-3495(02)75169-2

14 Nomura, T. *et al.* Differential effects of lipids and lyso-lipids on the mechanosensitivity of the mechanosensitive channels MscL and MscS. *Proceedings of the National Academy of Sciences* **109**, 8770-8775 (2012). https://doi.org/doi:10.1073/pnas.1200051109

15 Akitake, B., Anishkin, A., Liu, N. & Sukharev, S. Straightening and sequential buckling of the pore-lining helices define the gating cycle of MscS. *Nat Struct Mol Biol* **14**, 1141-1149 (2007).

16 Akitake, B., Anishkin, A. & Sukharev, S. The "Dashpot" Mechanism of Stretch-dependent Gating in MscS. *JGP* **125**, 143-154 (2005). https://doi.org/10.1085/jgp.200409198

17 Kamaraju, K., Belyy, V., Rowe, I., Anishkin, A. & Sukharev, S. The pathway and spatial scale for MscS inactivation. *JGP* **138**, 49-57 (2011).

18 Çetiner, U., Anishkin, A. & Sukharev, S. Spatiotemporal relationships defining the adaptive gating of the bacterial mechanosensitive channel MscS. *Eur Biophys J* **47**, 663-677 (2018). https://doi.org/10.1007/s00249-018-1303-5

19 Britt, M., Moller, E., Maramba, J., Anishkin, A. & Sukharev, S. MscS inactivation and recovery are slow voltage-dependent processes sensitive to interactions with lipids. *Biophys. J.* **123**, 195-209 (2024). https://doi.org/https://doi.org/10.1016/j.bpj.2023.12.007

20 Boer, M., Anishkin, A. & Sukharev, S. Adaptive MscS gating in the osmotic permeability response in E. coli: the question of time. *Biochemistry* **50**, 4087-4096 (2011).

21 Rowe, I., Anishkin, A., Kamaraju, K., Yoshimura, K. & Sukharev, S. The cytoplasmic cage domain of the mechanosensitive channel MscS is a sensor of macromolecular crowding. *J Gen Physiol* **143**, 543-557 (2014). https://doi.org/10.1085/jgp.201311114

22 Belyy, V., Anishkin, A., Kamaraju, K., Liu, N. & Sukharev, S. The tension-transmitting 'clutch' in the mechanosensitive channel MscS. *Nat. Struct. Mol. Biol.* **17**, 451-458 (2010).

23 Sukharev, S. I., Martinac, B., Arshavsky, V. Y. & Kung, C. Two types of mechanosensitive channels in the Escherichia coli cell envelope: solubilization and functional reconstitution. *Biophys J* **65**, 177-183 (1993). https://doi.org/10.1016/s0006-3495(93)81044-0

24 Ridone, P., Nakayama, Y., Martinac, B. & Battle, A. R. Patch clamp characterization of the effect of cardiolipin on MscS of E. coli. *Eur Biophys J* **44**, 567-576 (2015). https://doi.org/10.1007/s00249-015-1020-2

25 Anishkin, A. & Sukharev, S. Water dynamics and dewetting transitions in the small mechanosensitive channel MscS. *Biophys.J.* **86**, 2883-2895 (2004).

26 Flegler, V. J. *et al.* Mechanosensitive channel gating by delipidation. *PNAS* **118**, e2107095118 (2021). https://doi.org/doi:10.1073/pnas.2107095118

27 Reddy, B., Bavi, N., Lu, A., Park, Y. & Perozo, E. Molecular basis of force-from-lipids gating in the mechanosensitive channel MscS. *eLife* **8** (2019). https://doi.org/10.7554/eLife.50486

28 Zhang, Y. *et al.* Visualization of the mechanosensitive ion channel MscS under membrane tension. *Nature* **590**, 509-514 (2021). https://doi.org/10.1038/s41586-021-03196-w

29 Rasmussen, T., Flegler, V. J., Rasmussen, A. & Böttcher, B. Structure of the Mechanosensitive Channel MscS Embedded in the Membrane Bilayer. *J. Mol. Biol.* **431**, 3081-3090 (2019). https://doi.org/https://doi.org/10.1016/j.jmb.2019.07.006

30 Angiulli, G. *et al.* New approach for membrane protein reconstitution into peptidiscs and basis for their adaptability to different proteins. *eLife* **9**, e53530 (2020). https://doi.org/10.7554/eLife.53530

31 Wang, W. *et al.* The structure of an open form of an *E. coli* mechanosensitive channel at 3.45 A resolution. *Science* **321**, 1179-1183 (2008). https://doi.org/10.1126/science.1159262

32 Lai, J. Y., Poon, Y. S., Kaiser, J. T. & Rees, D. C. Open and shut: crystal structures of the dodecylmaltoside solubilized mechanosensitive channel of small conductance from *Escherichia coli* and *Helicobacter pylori* at 4.4 Å and 4.1 Å resolutions. *Protein Sci* **22**, 502-509 (2013). https://doi.org/10.1002/pro.2222

33 Park, Y. C., Reddy, B., Bavi, N., Perozo, E. & Faraldo-Gómez, J. D. State-specific morphological deformations of the lipid bilayer explain mechanosensitive gating of MscS ion channels. *eLife* **12**, e81445 (2023). https://doi.org/10.7554/eLife.81445

34 Pliotas, C. *et al.* The role of lipids in mechanosensation. *Nat Struct Mol Biol* **22**, 991-998 (2015). https://doi.org/10.1038/nsmb.3120

35 Pliotas, C. & Naismith, J. H. Spectator no more, the role of the membrane in regulating ion channel function. *Current opinion in structural biology* **45**, 59-66 (2017). https://doi.org/10.1016/j.sbi.2016.10.017

36 Moller, E. *et al.* Mechanosensitive channel MscS is critical for termination of the bacterial hypoosmotic permeability response. *J Gen Physiol* **155** (2023). https://doi.org/10.1085/jgp.202213168

37 Ramsey, K. *et al.* The dynamic hypoosmotic response of *Vibrio cholerae* relies on the mechanosensitive channel MscS. *iScience* **27** (2024). https://doi.org/10.1016/j.isci.2024.110001

38 Danielczak, B. *et al.* A bioinspired glycopolymer for capturing membrane proteins in native-like lipid-bilayer nanodiscs. *Nanoscale* **14**, 1855-1867 (2022). https://doi.org/10.1039/D1NR03811G

39 Choy, B. C., Cater, R. J., Mancia, F. & Pryor, E. E. A 10-year meta-analysis of membrane protein structural biology: Detergents, membrane mimetics, and structure determination techniques. *Biochimica et Biophysica Acta (BBA) - Biomembranes* **1863**, 183533 (2021). https://doi.org/https://doi.org/10.1016/j.bbamem.2020.183533

40 Guo, Y. Detergent-free systems for structural studies of membrane proteins. *Biochemical Society Transactions* **49**, 1361-1374 (2021). https://doi.org/10.1042/bst20201080

41 Qiu, W. *et al.* Structure and activity of lipid bilayer within a membrane-protein transporter. *Proceedings of the National Academy of Sciences* **115**, 12985-12990 (2018). https://doi.org/doi:10.1073/pnas.1812526115

42 Sun, C. *et al.* Structure of the alternative complex III in a supercomplex with cytochrome oxidase. *Nature* **557**, 123-126 (2018). https://doi.org/10.1038/s41586-018-0061-y

43 Knowles, T. J. *et al.* Membrane Proteins Solubilized Intact in Lipid Containing Nanoparticles Bounded by Styrene Maleic Acid Copolymer. *Journal of the American Chemical Society* **131**, 7484-7485 (2009). https://doi.org/10.1021/ja810046q

44 Higgins, A. J. *et al.* Cycloalkane-modified amphiphilic polymers provide direct extraction of membrane proteins for CryoEM analysis. *Communications Biology* **4**, 1337 (2021). https://doi.org/10.1038/s42003-021-02834-3

45 Brohawn, S. G., Campbell, E. B. & MacKinnon, R. Physical mechanism for gating and mechanosensitivity of the human TRAAK K+ channel. *Nature* **516**, 126-130 (2014). https://doi.org/10.1038/nature14013

46 Kern, D. M. *et al.* Structural basis for assembly and lipid-mediated gating of LRRC8A:C volume-regulated anion channels. *Nature Structural & Molecular Biology* **30**, 841-852 (2023). https://doi.org/10.1038/s41594-023-00944-6

47 Cronan, J. E., Jr. & Rock, C. O. Biosynthesis of Membrane Lipids. *EcoSal Plus* **3** (2008). https://doi.org/10.1128/ecosalplus.3.6.4

48 Lennen, R. M., Politz, M. G., Kruziki, M. A. & Pfleger, B. F. Identification of Transport Proteins Involved in Free Fatty Acid Efflux in Escherichia coli. *Journal of Bacteriology* **195**, 135-144 (2013). https://doi.org/10.1128/jb.01477-12

49 Yang, H. *et al.* Lipid A Structural Determination from a Single Colony. *Anal Chem* **94**, 7460-7465 (2022). https://doi.org/10.1021/acs.analchem.1c05394

50 Lennen, R. M. & Pfleger, B. F. Engineering Escherichia coli to synthesize free fatty acids. *Trends Biotechnol* **30**, 659-667 (2012). https://doi.org/10.1016/j.tibtech.2012.09.006

51 Çetiner, U., Raz, O., Britt, M. & Sukharev, S. Dissipation during the Gating Cycle of the Bacterial Mechanosensitive Ion Channel Approaches the Landauer Limit. *Entropy* **25**, 779 (2023).

52 Sotomayor, M., Vasquez, V., Perozo, E. & Schulten, K. Ion conduction through MscS as determined by electrophysiology and simulation. *Biophys J* **92**, 886-902 (2007).

53 Skulachev, V. P. Chemiosmotic systems in bioenergetics: H(+)-cycles and Na(+)-cycles. *Biosci Rep* **11**, 387-441; discussion 441-384 (1991).

54 Felle, H., Porter, J. S., Slayman, C. L. & Kaback, H. R. Quantitative measurements of membrane potential in Escherichia coli. *Biochemistry* **19**, 3585-3590 (1980). https://doi.org/10.1021/bi00556a026

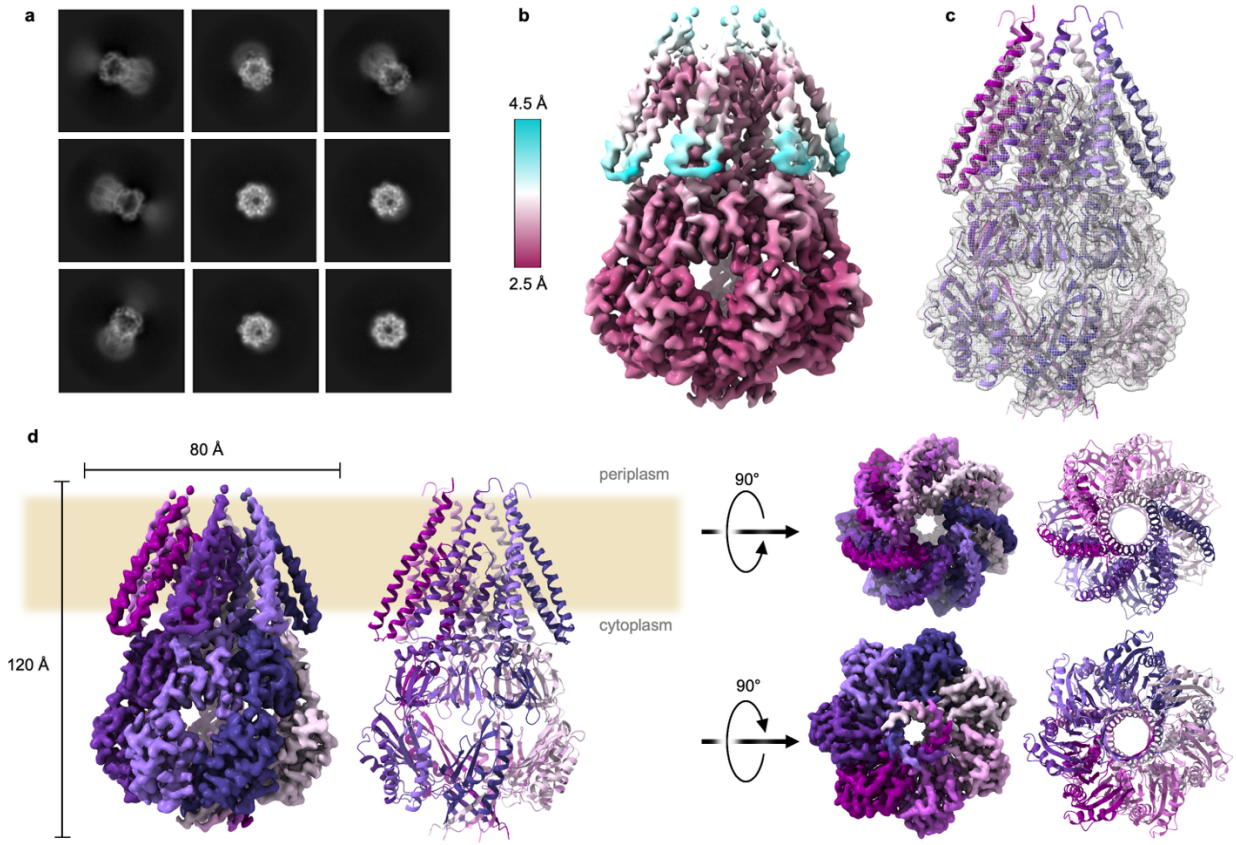

Fig. 1: *E. coli* MscS cryo-EM structure in Glyco-DIBMA. (a) Selected 2D class averages of the particles used for the final reconstruction with a box size of 360 px (~300 Å). (b) Cryo-EM map filtered and colored by local resolution. (c) Fitted model in ribbon representation inside map shown in gray mesh. (d) Map and model colored by chain shown as side view (left), top, and bottom view (right).

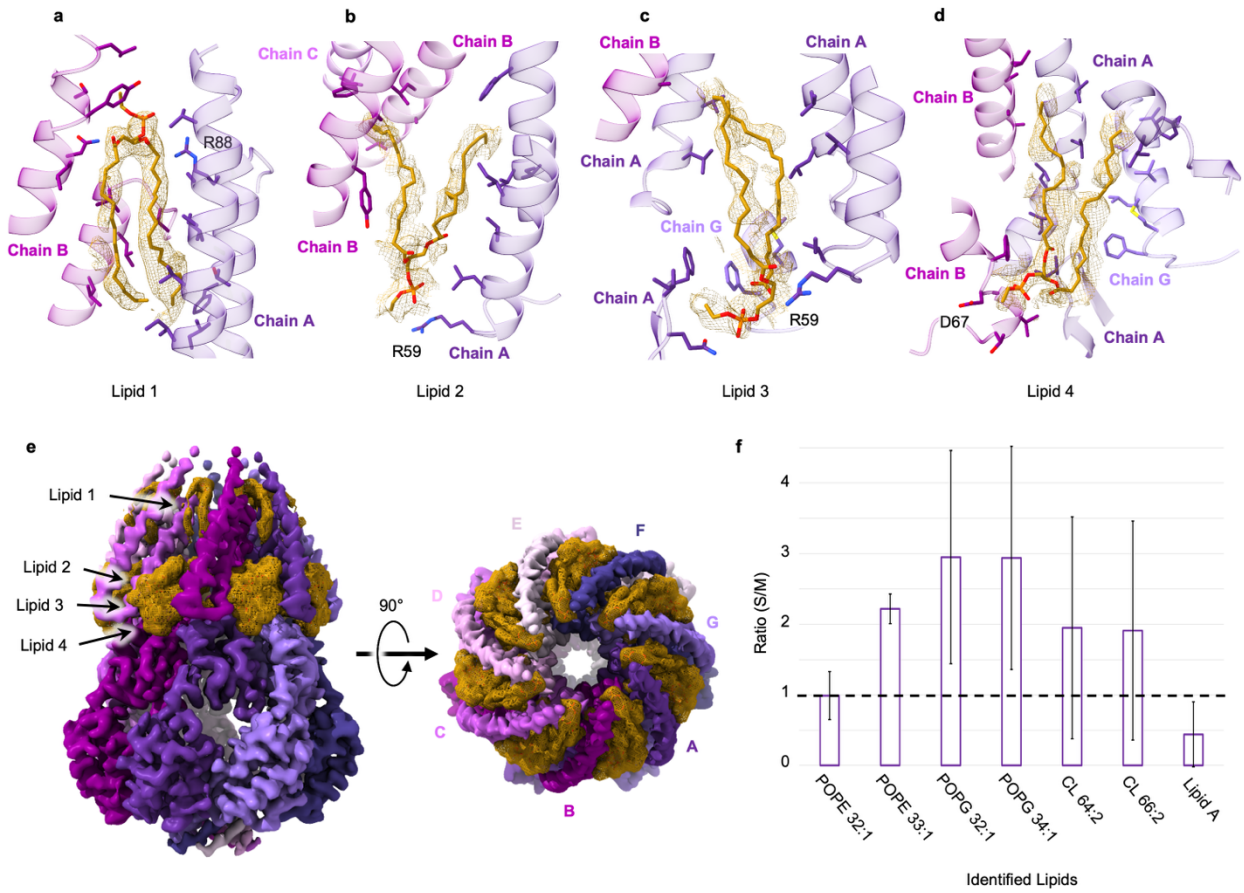

Fig. 2: Resolved lipids in the TM region of *E. coli* MscS and lipid mass spectrometry analysis. Lipid 1 (a), Lipid 2 (b), Lipid 3 (c) and Lipid 4 (d) in yellow mesh density shown with all residues within 5 Å within the modeled protein. A full list of nearby residues is given in Extended Data Table 1. (e) Full map colored by chain with lipid densities shown in yellow mesh, side and top view. (f) Histogram comparing the relative amounts of lipids between the protein sample isolated in native nanodiscs (S) and the total inner membrane fraction (M). The ratio of mole fractions of specific lipids in these two samples (S/M) shows that POPE 33:1 and the two POPGs are enriched (1.5- to 2-fold), whereas other lipids, including POPE 32:1, are not. Cardiolipins are slightly enriched, whereas lipid A is depleted. Error shown is standard deviation. Exact values from this histogram are given in Extended Data Table 2.

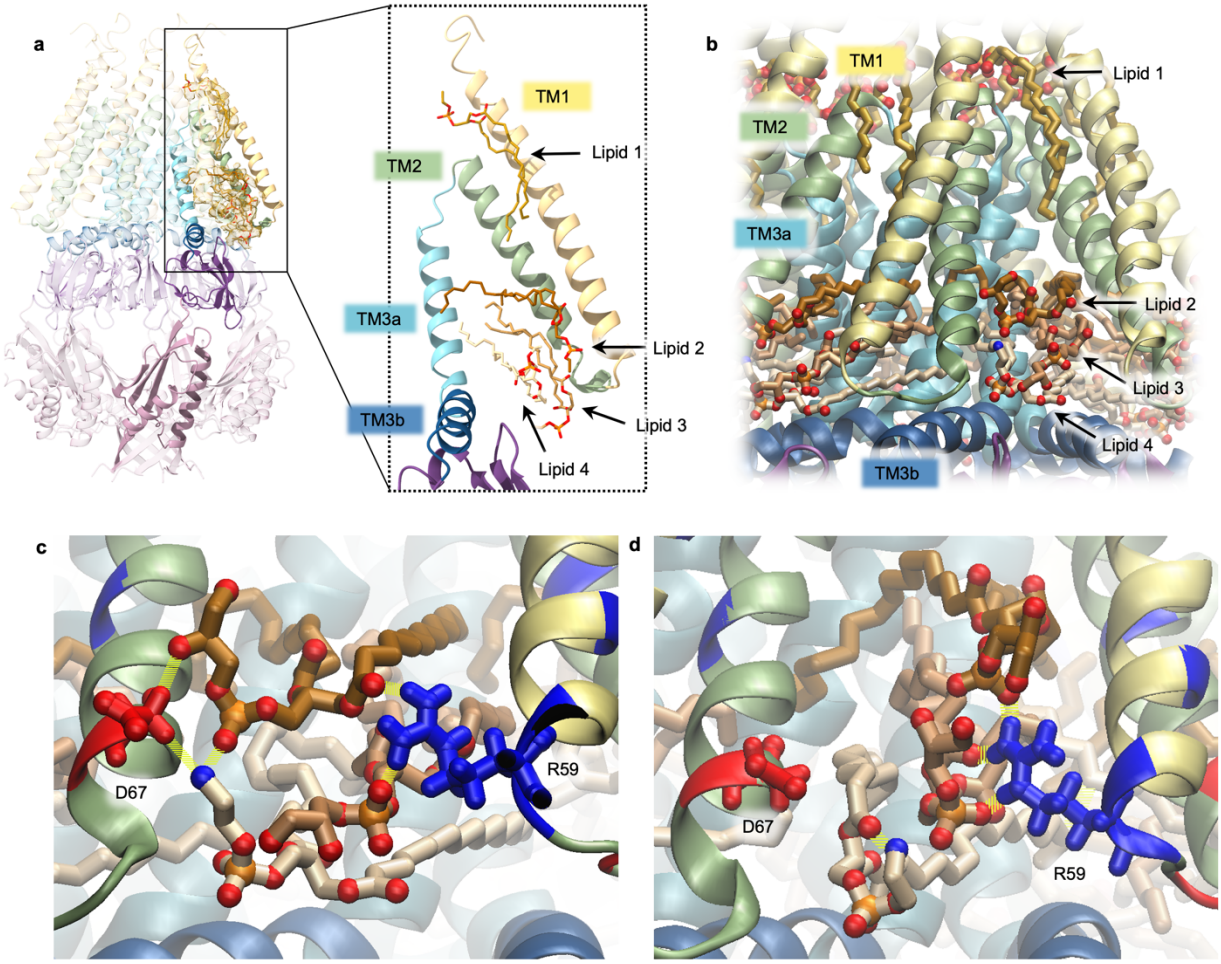

Fig. 3: Molecular dynamics simulations of lipids in MscS's interhelical crevices. (a) The model of MscS built into the cryo-EM density with the resolved lipids, colored by domain with TM1 in yellow, TM2 in green, TM3a in cyan, and TM3b in blue. (b) A snapshot from MD simulations of the modeled lipids showing lipid tail penetration between TM1-TM2 pairs (yellow and green) and pore-forming TM3a (cyan). (c-d) Zoomed-in snapshots illustrating two different lipid clusters stabilized by inter-lipid H-bonds and coordinated between D67 and R59. The clusters appear to be both flexible and stable due to their multitude of configurations. Lipids are shaded from dark to light: Lipid 2 (dark), Lipid 3 (medium), and Lipid 4 (light). The statistics of intercalated lipid contacts in interhelical crevices with neighboring residues are listed in Extended Data Table 3.

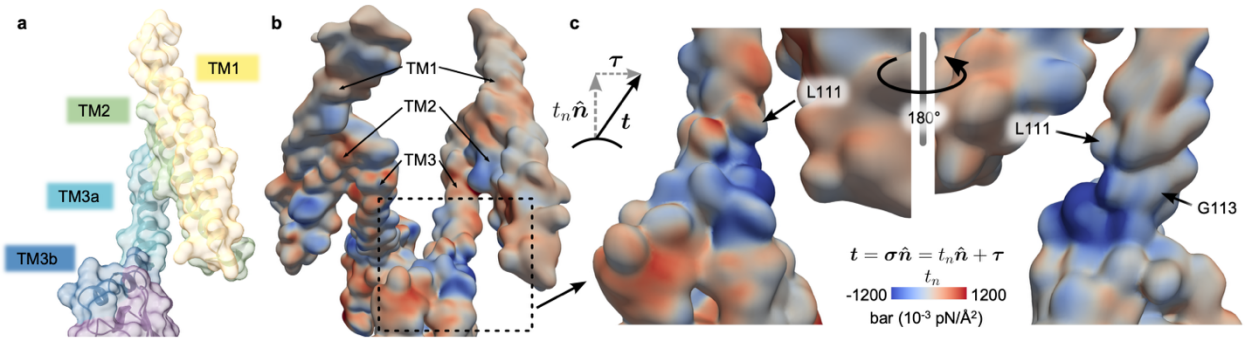

Fig. 4: Computation of local 3D stress acting on the protein surface of the lipid-embedded MscS. Stress on the surface of individual MscS chains is visualized through the traction vector, $\boldsymbol{t} = \boldsymbol{\sigma}\hat{\boldsymbol{n}}$, which is obtained from the product of the local stress tensor ($\boldsymbol{\sigma}$) and the normal unit vector ($\hat{\boldsymbol{n}}$) defined by the protein surface. (a) MscS surface colored by domain. (b) Normal component of the traction ($t_n = \boldsymbol{t} \cdot \hat{\boldsymbol{n}}$) on chains A (left) and E (right) of the simulation showing the distribution of forces on TM1, TM2, and TM3. (c) Close-up of chain E in the vicinity of the kink in TM3 near residues L111 and G113. Blue colors indicate forces pushing into the surface, while red colors indicate pulling forces. The surface of the MscS chains is computed as isosurfaces from the average mass density of the protein.

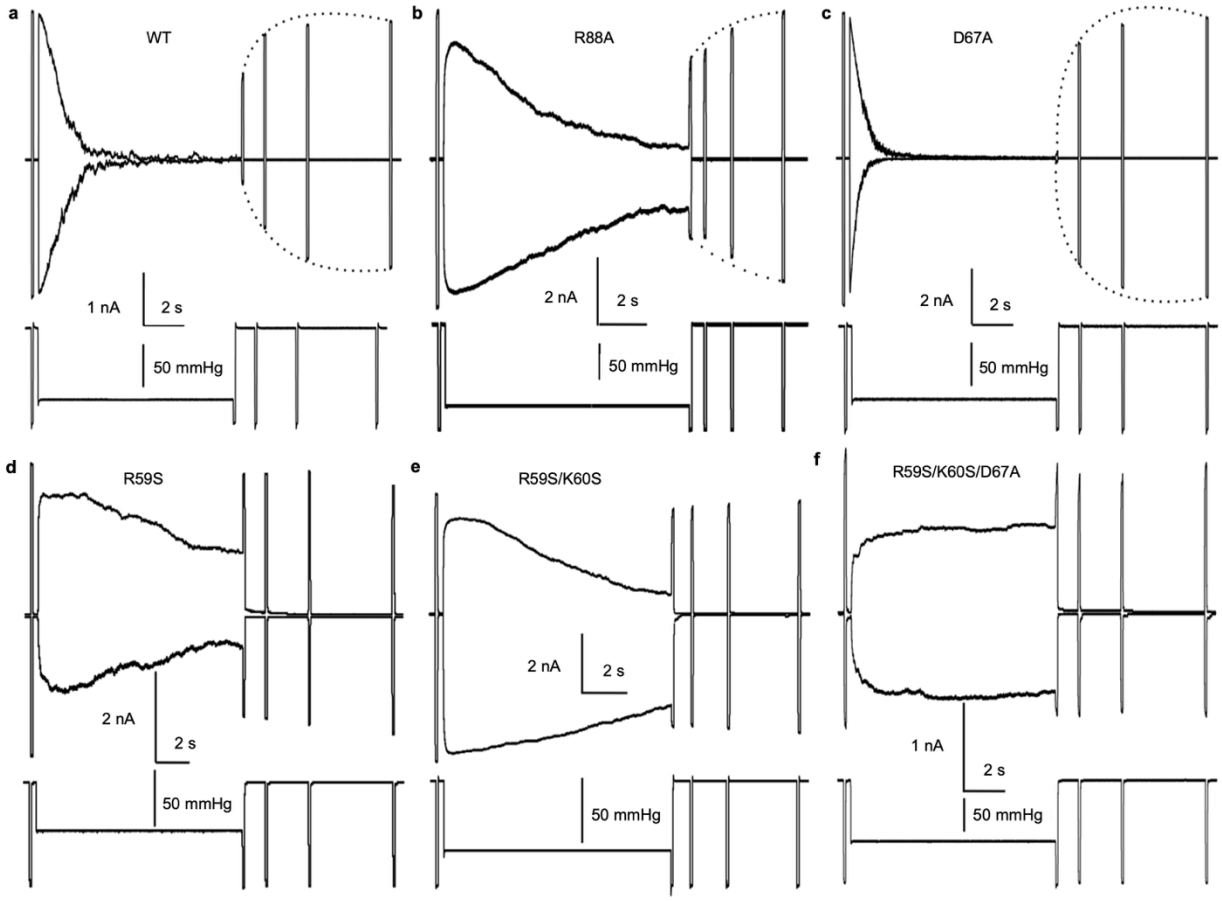

Fig. 5: Patch-clamp traces examining inactivation and recovery. The first short test pulse of saturating amplitude opens the entire population of channels, then the extended step of intermediate tension drives them toward inactivation. The following train of saturating test pulses monitors the fraction of remaining active channels, which is used to determine the kinetics of recovery. R88A (b) behaves similarly to WT (a). The D67A mutant (c) inactivates completely and recovers very quickly, whereas R59S (d) is mainly resistant to inactivation. The double mutant (e) and triple mutant (f) follow the R59S Inactivation/Recovery phenotype. The triple mutant is also resistant to adaptive closing at the midpoint tension.

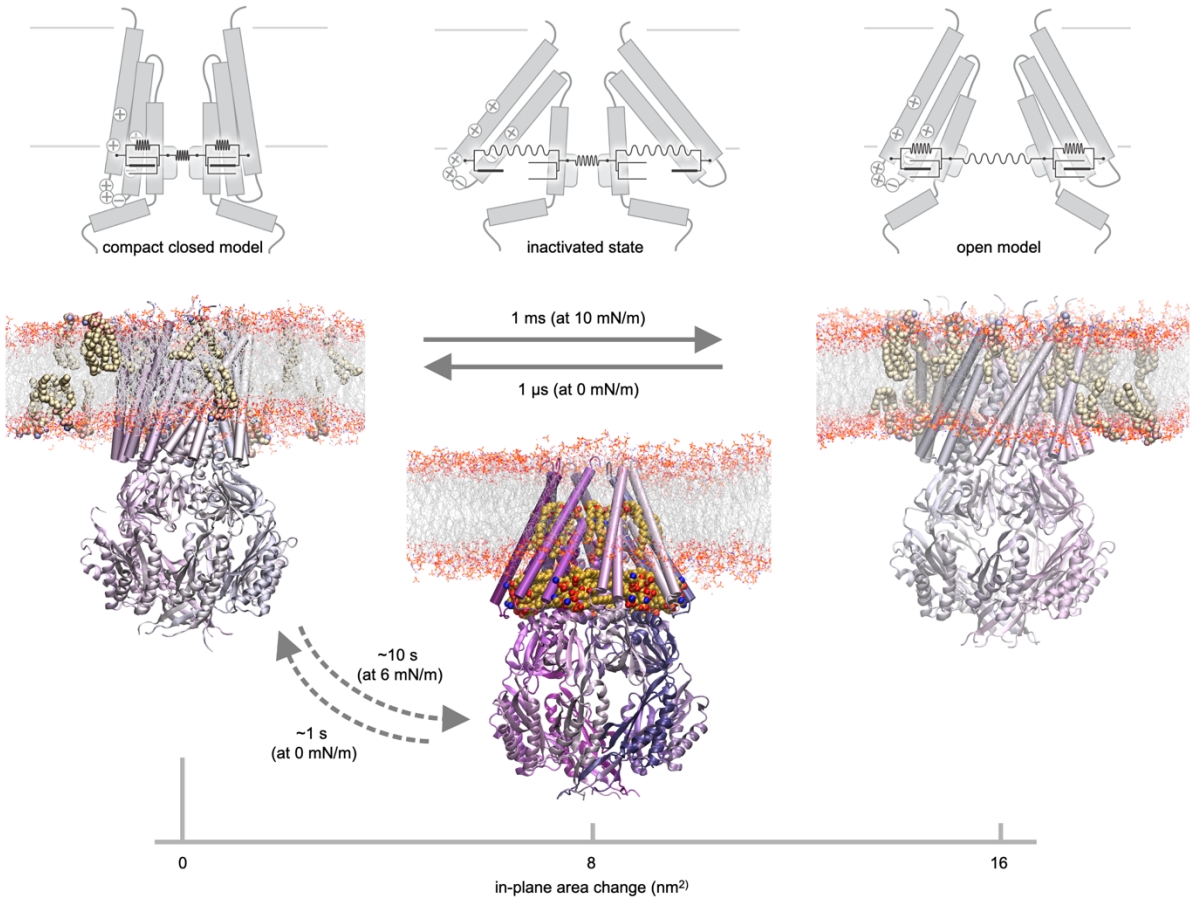

Fig. 6: The experimentally determined kinetic scheme of MscS and the assignment of the newly solved structure. The opening-closing and inactivation-recovery pathways are characterized by different spatial scales and drastically different characteristic times of transitions. The solved cryo-EM structure, filled with native lipids, fits all the criteria of the inactivated state. The transition to the inactivated state from the closed state is accompanied by moderate in-plane protein expansion and occurs at near-threshold tensions. The opening from the hypothetical compact closed state is associated with a larger lateral expansion at higher tensions. The gating scheme implies a sharp kinetic separation between the opening and inactivation pathways.

581 **Methods**

582 *MscS Expression and Inner Membrane Isolation*

583 *E. coli* MscS wild-type (WT) was expressed in MJF465 cells (Frag1 ΔmscL::Cm, ΔyggB, ΔmscK::kan) [1]
584 from the pB10d vector, a modified pB10b plasmid [55]. The plasmid is Isopropyl β-D-thiogalactopyranoside
585 (IPTG) inducible with the lac UV5 and lacIq promoters, confers ampicillin resistance, and includes a C-
586 terminal His6-tag on the MscS gene. It uses the high-copy-number ColE1/pMB1/pBR322/pUC origin of
587 replication and the T7 bacteriophage ribosome binding site. The MJF465 strain originated from the Ian
588 Booth laboratory (University of Aberdeen, Aberdeen, UK) was provided by Dr. Samantha Miller
589 (University of Aberdeen). A single colony of the plasmid-containing strain was inoculated into 35 mL
590 Lysogeny Broth (LB) media supplemented with 100 µg/mL Ampicillin (Amp) and grown overnight. 5 mL
591 of the overnight culture was sub-cultured into six 2 L flasks containing 1 L LB supplemented with Amp
592 and grown for 2 hours shaking at 225 rpm at 30ºC to an OD600 of approximately 0.3 before induction
593 with 1 mM IPTG for an additional 3 hours to a final OD600 of 2.0. When the target OD was achieved,
594 cells were placed on ice to prevent further growth, pelleted at 7,000 rpm using Sorvall GSA rotor for 15
595 min at 4ºC, and resuspended in French Press Buffer (20 mM Tris/HCl pH 7.6, 150 mM NaCl)
596 supplemented with 200 µL saturated PMSF in EtOH to 30 mL total volume before rupturing with a
597 French press. Unbroken cells were pelleted by centrifugation at 10,000 rpm using Eppendorf F-34-6-38
598 rotor for 15 min at 4ºC, and the supernatant was then ultracentrifuged at 25,000 rpm using Beckman
599 SW28 rotor (112,400 x g) for 1 hour at 4ºC to pellet membranes. Supernatant was discarded, and
600 membranes were resuspended in 20% [w:v] sucrose prepared in Gradient Buffer (20 mM HEPES pH 7.2,
601 5 mM EDTA) and homogenized before being placed on top of a 3-step sucrose gradient of 0.77 M, 1.44
602 M, and 2.02 M prepared in Gradient Buffer, and finally ultracentrifuged at 25,000 rpm using Beckman
603 SW28 rotor (112,400 x g) for 16 hours at 8ºC. The inner membranes were harvested from the upper band
604 of the gradient by puncturing the tube wall with a syringe needle, diluted in Gradient Buffer with no
605 sucrose to 70 mL total volume, and ultracentrifuged at 25,000 rpm using Beckman SW28 rotor (112,400 x
606 g) for 1 hour at 4ºC to re-pellet membranes. The membrane pellets were flash-frozen in liquid nitrogen
607 and stored at -80ºC until use.

608

609 *Polymer Extraction and Affinity Purification*

610 *E. coli* inner membranes were resuspended to 10 mg/ml in Membrane Buffer (20 mM HEPES pH 7.4, 100
611 mM NaCl) and homogenized before the addition of 0.5% [w:v] of solid Glyco-DIBMA [38] (Cube Biotech).
612 The first condition (Glyco-DIBMA #1) was allowed to extract overnight at 4ºC on the tube revolver,
613 while the second condition (Glyco-DIBMA #2) was allowed to extract for 2 hrs at room temperature on
614 the tube revolver. The insoluble fraction was then pelleted by ultracentrifugation at 25,000 rpm using

615 Beckman SW28 rotor (112,400 x g) for 35 min at 4ºC. The supernatant was then diluted 1:5 with
616 Membrane Buffer to improve binding efficiency and incubated overnight on the tube revolver at 4ºC with
617 TALON Cobalt Resin (Takara Bio). The next day the resin was washed with 10 column volumes of
618 Membrane Buffer, 10 column volumes of Wash Buffer (20 mM HEPES pH 7.4, 100 mM NaCl, 10%
619 glycerol [v:v]) with 10 mM imidazole, 5 column volumes Wash Buffer with 20 mM imidazole, and 5
620 column volumes of Wash Buffer with 40 mM imidazole before elution with Elution Buffer (20 mM
621 HEPES pH 7.4, 100 mM NaCl, 10% glycerol [v:v], 350 mM imidazole). Elution fractions were then
622 dialyzed with Membrane Buffer overnight to remove imidazole and glycerol and concentrated the
623 following day using a 100 kDa ultrafiltration membrane (Amicon) to the desired concentration for cryo-
624 EM grid preparation. Protein fractions were resolved and analyzed using SDS-PAGE, Western Blot, and
625 BN-PAGE (see Extended Data Methods); gel images and Western blots can be found in Extended Data
626 Fig. 3. Many different polymers are now commercially available; we have also attempted MscS extraction
627 using SMALP 200 [43] and CyclAPol C_8-C_0-50 [44], but these preparations did not allow us to resolve the
628 transmembrane domain of MscS (see Extended Data Text).
629
630 *Negative Staining Electron Microscopy*
631 3 µL of MscS sample at 0.3 mg/ml (30 times higher than MscS in detergents or mixed micelles of
632 typically ~ 0.01 mg/mL) was applied to a glow-discharged carbon coated 400 square mesh copper grid
633 (CF400-CU, EMS) and incubated for 1 min at room temperature. The grid was then blotted by filter paper
634 (Whatman Grade 2) and washed once with 3 µL of Nano-W negative staining solution (Nanoprobes)
635 followed by incubation with 3 µL of Nano-W for 1 min. The grid was blotted to remove excess staining
636 solution and air dried by waving for an additional minute. Images were recorded using an FEI Tecnai T20
637 TEM operated at 200 kV with a direct electron detector K2 Summit (Gatan Inc). Data was collected using
638 SerialEM [56] at a nominal magnification of 25,000x with a pixel size of 1.479 Å/px, a dose rate of
639 approximately 7 e^-/px/s with 0.2 s frames over 10 s, and a defocus range between -1.3 and -2 µm. A total
640 of 651 images were collected, and Bsoft 2.2.0 [57] was used to unpack the image stacks. Image processing
641 was performed using cisTEM v1.0.0. [58]. 37,902 particles were picked from the micrographs after CTF
642 estimation [59] using a maximum radius of 60 Å and a characteristic radius of 40 Å with a threshold of 5.
643 Particles were extracted with a box size of 168 px (~250 Å) and analyzed using 2D classification
644 (Extended Data Fig. 3p-r). 2D class averages and data collection parameters for MscS extracted with
645 SMALP 200 [43] and CyclAPol C_8-C_0-50 [44] can be found in Extended Data. Negative staining micrographs
646 for the polymers alone in buffer (see Extended Data Methods) are illustrated in Extended Data Fig. 6.
647
648 *Cryo-EM Grid Preparation and Data Collection*

649 3 µL of purified MscS between 0.1 and 0.7 mg/mL was applied to a glow-discharged (15 s at 15 mA using
650 EasyGlow) Quantifoil R 1.2/1.3 + 2 nm C 400 Cu mesh grid (EMS), a holey grid with a thin 2 nm
651 continuous carbon film. The grids were blotted for 6 s at 4°C and 95% humidity and plunged frozen into
652 liquid ethane using a Leica EM GP2 (Leica) and stored in liquid nitrogen. For the Glyco-DIBMA
653 extracted MscS, a double sample application was performed where 3 µL of the sample was applied,
654 blotted by hand using Whatman Grade 2 filter paper, then 3 µL was re-applied and blotted using a Leica
655 EM GP2. The grids were screened on an FEI Tecnai T20 TEM before data collection. Cryo-EM datasets
656 were acquired with SerialEM [56] using a G1 or G4 Titan Krios (FEI, now ThermoFisher Scientific)
657 operated at 300 kV and equipped with an energy filter and K3 camera (Gatan Inc.). Movies of 50-60
658 frames were collected with a total dose of 50 $e^-/Å^2$ at a nominal magnification of 105,000x corresponding
659 to a physical pixel size of 0.83 or 0.8469 Å/px at a dose rate of 9-15 e^-/px/s and a defocus range of -0.8 to
660 -1.8 µm. Specific collection parameters for each dataset can be found in Extended Data Table 6.
661
662 *Cryo-EM Data Processing*
663 The specific workflows for image processing are illustrated in Extended Data Fig. 7-11. All processing
664 was performed with cryoSPARC v3.3.250 [60]. Movies were processed with patch motion correction [61] and
665 patch CTF estimation [59]. Blob picker was used for the majority of particle picking, and particles were
666 extracted with a box size of 320-360 px (~300 Å) and subjected to 2D classification to remove junk
667 particles. Selected particles were used for ab initio reconstruction, heterogeneous refinement, and non-
668 uniform refinement using no symmetry (C1) as well as 7-fold symmetry (C7) [62]. The local resolution was
669 estimated, and the maps were filtered accordingly. Additional CTF refinements and local motion
670 correction did not improve resolution, most likely because the 2 nm carbon layer support already reduces
671 beam-induced motion [63].
672
673 *Model Building and Refinement*
674 For the MscS atomic model, PDB 7OO6 [26] was rigid body-fitted into the sharpened local resolution
675 filtered map using UCSF ChimeraX v.1.8 [64]. The model was then manually rebuilt in COOT v.0.9.8.92 [65]
676 using the same map, which was generated from non-uniform refinement with C7 applied. The truncated
677 lipid was generated using the SMILES string CCCCCCCCCCCCCCCC(=O)OCC(COP([O-
678])(=O)OCC)OC(=O)CCCCCCC\C=C\CCCCCCCC in eLBOW [66]. Iterative rounds of manual refinement
679 in COOT and real space refinement in Phenix v.1.21.2-5419 [67] were performed. The quality of the model
680 and fit to the density was assessed using MolProbity [68] and Phenix [67]. Side chain densities for a helix and
681 beta sheet are shown in Extended Data Fig. 12. In contrast to the structured helix reported in 6PWN [27] and
682 6YVK [28], the N-terminal residues are poorly resolved until residue 17, indicating that they are flexible

683 and disordered. The protein was modeled from residue 17 to 281 out of the 287 total residues (Fig. 1c),
684 with the side chains removed from residues 17, 18, 20, 21, 280, and 281 due to low density. All structural
685 figures were prepared using UCSF ChimeraX v.1.8 [64]. Cryo-EM map and model analysis values are listed
686 in Extended Data Table 7. PDBs have been made available together with the cryo-EM maps with the
687 following EMD/PDB IDs: EMD-71088/7P0N for the MscS/Glyco-DIBMA (C7) and EMD-71089/7P0O
688 for the MscS/Glyco-DIBMA (C1). Movies as well as particle stacks have been uploaded to EMPIAR [69].
689
690 *FLAT-MS for lipid analysis*
691 The MscS sample for Mass Spectrometry (MS) lipid analysis to identify co-purified lipids was prepared
692 as described for Glyco-DIBMA #2, with an additional gel filtration step using a hand-packed column
693 containing Sephacryl S-200 Superfine (Pharmacia Fine Chemicals). No dialysis was performed, the
694 sample was exchanged into Membrane Buffer (20 mM HEPES pH 7.4, 100 mM NaCl) on the column.
695 The SDS-PAGE, Western Blot, and Negative Staining micrographs from this purification showing the
696 removal of large lipid patches with size exclusion can be found in Extended Data Fig. 4c-f. The control
697 sample is purified *E. coli* inner membranes (see *MscS Expression and Inner Membrane Isolation)*
698 resuspended in Membrane Buffer. An initial round of MS without this additional separation step was done
699 on the remaining protein sample after cryo-EM grid preparation, but it showed no dramatic lipid
700 enrichment since the ratios were skewed by the large membrane sections rather than examining only the
701 lipids immediately surrounding MscS (See Extended Data Fig. 4). 1 µL of sample pellet was scraped and
702 plated directly onto a steel reusable MALDI plate. 1 µL of citric acid extraction buffer (0.2 M citric acid,
703 0.1 M trisodium citrate, pH 3.5) was spotted on top of the plated sample. The steel MALDI plate was
704 placed into the chamber with water on the bottom and heated to 110ºC in an oven for 30 minutes. After
705 incubation, the plate was rinsed with water and air-dried, and 1 µL of norharmane matrix was spotted on
706 each sample. A Bruker Matrix-Assisted Laser Desorption/Ionization trapped ion mobility spectrometry
707 Time-of-Flight Mass Spectrometry MALDI (tims TOF) MS was used for the Fast Lipid Analysis
708 Technique (FLAT), a protocol for direct MS biomass visualization of lipid A and phospholipids [70] as
709 described below.
710
711 Our Bruker MALDI (tims TOF) spectrometer is equipped with a dual ESI/MALDI source with a
712 SmartBeam3D 10 kHz frequency tripled Nd:YAG laser (355 nm); the system was operated in "qTOF"
713 mode (TIMS deactivated) for these experiments. Ion transfer tuning was used with the following
714 parameters: funnel1 RF, 440.0 Vpp; funnel2 RF,490.0 Vpp; multipole RF, 490.0 Vpp; CID energy, 0.0 eV;
715 and deflection delta, -60.0 V. Quadrupole was used with the following values for MS mode: ion energy,
716 4.0 eV. The m/z scan range for MS is set to 1000 to 3000. Collision cell activation of ions used the

717 following values for MS mode: collision energy, 9.0 eV; collision RF, 3900.0 Vpp. Agilent ESI tune mix
718 was used to perform calibration of the m/z scale. MALDI parameters in qTOF were optimized to
719 maximize intensity by tuning ion optics, laser intensity, and laser focus. All spectra were collected at a
720 104 μm laser diameter with a beam scan using 800 laser shots per spot and 70 and 80% laser power,
721 respectively.
722
723 MS data were collected in negative ion mode. In all cases, 10 mg/mL of norharmane (NRM) in 1:2
724 MeOH/CHCl3 [v:v] was used for lipid detection. All MALDI (tims TOF) data were visualized using
725 mMass (Ver 5.5.0). Peak picking was conducted in mMass using the following parameters: S/N threshold:
726 3.0; relative intensity threshold: 5.0%; picking height: 50; apply baseline and smoothing. For the triplicate
727 experiment, we analyzed the samples on three different days, obtaining a total of nine mass spectra for
728 both purified inner membrane and MscS protein samples. These spectra were analyzed using mMass to
729 determine the average relative intensity values for each of the seven assigned lipids. Standard deviations
730 for each lipid intensity were calculated using Microsoft Excel.
731
732 *Molecular Dynamics Simulations*
733 The simulation system was assembled around our cryo-EM structure with three POPG and one POPE per
734 subunit based on the enrichment observed in mass spectrometry. The lipid bilayer built with 498 POPE
735 and 166 POPG molecules (ratio 3/1) was assembled around the channel to bring the lateral size of the
736 orthogonal simulation cell to 150 x 150 Å, allowing for at least 9-10 lipid layers between the closest
737 mirror images of the protein. The membrane protein system was hydrated, and K^+ and Cl^- ions were
738 added to make 200 mM KCl salt solution, bringing the total number of atoms in the system to ~395,000.
739 The simulation cell was assembled using CHARMM GUI [71]. The entire system was energy minimized
740 with a restrained protein backbone for 10,000 steps using the conjugate energy gradient algorithm and
741 simulated for 20 ns with the protein backbone harmonically restrained near the modeled positions with a
742 spring constant of 1 kcal/mol/Å. A flexible orthogonal cell was simulated with periodic boundary
743 conditions under 1 bar pressure and a lateral tension of 20 dyne/cm. All simulations were performed using
744 NAMD2 [72] with CHARMM27 force field [73], TIP3P water model, particle mesh Ewald method for long-
745 range electrostatics estimation [74], a 10 Å cutoff for short range electrostatic and Van der Waals forces, and
746 a Langevin thermostat set at 310 K. After the restrained backbone stage completed, the system was
747 simulated unrestrained for 100 ns, with the last 80 ns used to quantify the contact statistics. Visualization
748 of the channel structures was performed using Visual Molecular Dynamics (VMD) [75]. All the structural
749 and statistical analyses for MD simulations were performed using custom-written Tcl scripts for VMD.
750

751 To compute the local stress/pressure in 3D, the equilibrated systems were converted to GROMACS [76]
752 input files and simulated with version 2023 of the program for 50 ns, saving the positions and velocities
753 to the trajectory every 5 ps. The saved trajectory was first re-centered around the center of mass of the
754 protein to account for spontaneous lateral diffusion of the protein and then post-processed using the
755 GROMACS-LS and MDStress library [77,78]. This post-processing step produced a time-averaged 3D stress
756 field for each system using a grid spacing of 0.2 nm and an electrostatics cutoff of 2.2 nm. The 3D local
757 stress was then mapped onto the surface of the MscS individual chains by computing the traction vector
758 ($\boldsymbol{t} = \boldsymbol{\sigma}\hat{\boldsymbol{n}}$) as the product of the stress tensor ($\boldsymbol{\sigma}$) with the surface normal unit vector $\hat{\boldsymbol{n}}$ as previously
759 reported [79]. The protein surface and normal vectors were obtained by computing the isosurface of the 3D
760 protein mass density. For ease of visualization, we only show the normal component of the traction vector
761 ($t = \boldsymbol{t} \cdot \hat{\boldsymbol{n}}$). The traction data was visualized using the ParaView software [80].
762
763 *Mutagenesis and Patch-clamp Electrophysiology*
764 Point mutations were introduced to the MscS plasmid using the Q5 site-directed mutagenesis kit (New
765 England Biolabs). Giant spheroplasts were generated as described previously [81]. In short, cells were
766 grown in LB to turbidity and then sub-cultured 1:9 into a defined minimal LB at 250 mOsm and grown
767 for 1.5 h in the presence of 0.06 mg/ml cephalexin, which prevents cell septation, before inducing with 1
768 mM IPTG for the final 30 min. The resulting filaments were transferred into 1 M sucrose with 1.8 mg/ml
769 BSA buffer and treated with 0.17 mg/ml lysozyme in the presence of 4 mM EDTA, which degrades the
770 peptidoglycan layer and causes the filaments to collapse into giant spheres. The reaction was stopped with
771 5 mM $MgCl_2$. The giant spheroplasts were isolated via sedimentation through a one-step 1.2 M sucrose
772 gradient at 2,000 rpm using Eppendorf Rotor A-4-81 for 5 min at 4ºC.
773
774 Patch-clamp traces were recorded from giant bacterial cell spheroplasts. Population channel recordings
775 were conducted at ±30 mV (pipette) on excised inside-out patches in symmetric buffer containing 400
776 mM sucrose, 200 mM KCl, 50 mM $MgCl_2$, 5 mM $CaCl_2$, and 5 mM HEPES at pH 7.4. Membrane
777 patches were obtained using borosilicate glass pipettes (Drummond) and recorded on an Axopatch 200B
778 amplifier (Molecular Devices). Negative pressure stimuli were applied using a high-speed pressure clamp
779 apparatus (HSPC-1; ALA Scientific) programmed using the Clampex software (Molecular Devices).
780 Pressure and voltage protocol programming and data acquisition were performed with the PClamp 10
781 suite (Axon Instruments). The patch responses were first recorded at +30 mV (pipette) with symmetric 1-
782 second pressure ramps to determine the activation thresholds, midpoints, and saturation level for the
783 plasmid expressed MscS population in both MJF465 (ΔMscL ΔMscS ΔMscK) and PB113 (ΔMscS
784 ΔMscK) where MscL is also present for comparison. PB113 is derived from the MJF429 strain [1] with the

785 additional ΔrecA [82] and was provided by Paul Blount (University of Texas at Dallas, Richardson, TX,
786 USA). MscL can be used as an internal standard with a known midpoint tension $\gamma_{0.5}$ = 14 mN/m and
787 midpoint ratio of 0.6, meaning that the ratio of the tension and the pressure midpoints between expressed
788 MscS and native MscL can be calculated [83]. To observe the inactivation of MscS, an
789 Inactivation/Recovery protocol was used [16,17,19]: the full population of channels was opened with a
790 saturating test pulse and then held at the midpoint tension for MscS for 10 s followed by three test pulses
791 with zero pressure steps in between. The rate of recovery (τ) was determined by fitting the recovery
792 pulses to a monoexponential function.

Methods References

1 Levina, N. *et al.* Protection of *Escherichia coli* cells against extreme turgor by activation of MscS and MscL mechanosensitive channels: identification of genes required for MscS activity. *EMBO J.* **18**, 1730-1737 (1999).

16 Akitake, B., Anishkin, A. & Sukharev, S. The "Dashpot" Mechanism of Stretch-dependent Gating in MscS. *JGP* **125**, 143-154 (2005). https://doi.org/10.1085/jgp.200409198

17 Kamaraju, K., Belyy, V., Rowe, I., Anishkin, A. & Sukharev, S. The pathway and spatial scale for MscS inactivation. *JGP* **138**, 49-57 (2011).

19 Britt, M., Moller, E., Maramba, J., Anishkin, A. & Sukharev, S. MscS inactivation and recovery are slow voltage-dependent processes sensitive to interactions with lipids. *Biophys. J.* **123**, 195-209 (2024). https://doi.org/https://doi.org/10.1016/j.bpj.2023.12.007

26 Flegler, V. J. *et al.* Mechanosensitive channel gating by delipidation. *PNAS* **118**, e2107095118 (2021). https://doi.org/doi:10.1073/pnas.2107095118

27 Reddy, B., Bavi, N., Lu, A., Park, Y. & Perozo, E. Molecular basis of force-from-lipids gating in the mechanosensitive channel MscS. *eLife* **8** (2019). https://doi.org/10.7554/eLife.50486

28 Zhang, Y. *et al.* Visualization of the mechanosensitive ion channel MscS under membrane tension. *Nature* **590**, 509-514 (2021). https://doi.org/10.1038/s41586-021-03196-w

38 Danielczak, B. *et al.* A bioinspired glycopolymer for capturing membrane proteins in native-like lipid-bilayer nanodiscs. *Nanoscale* **14**, 1855-1867 (2022). https://doi.org/10.1039/D1NR03811G

43 Knowles, T. J. *et al.* Membrane Proteins Solubilized Intact in Lipid Containing Nanoparticles Bounded by Styrene Maleic Acid Copolymer. *Journal of the American Chemical Society* **131**, 7484-7485 (2009). https://doi.org/10.1021/ja810046q

44 Higgins, A. J. *et al.* Cycloalkane-modified amphiphilic polymers provide direct extraction of membrane proteins for CryoEM analysis. *Communications Biology* **4**, 1337 (2021). https://doi.org/10.1038/s42003-021-02834-3

55 Iscla, I., Wray, R. & Blount, P. On the structure of the N-terminal domain of the MscL channel: helical bundle or membrane interface. *Biophys J* **95**, 2283-2291 (2008).

56 Mastronarde, D. N. Automated electron microscope tomography using robust prediction of specimen movements. *J Struct Biol* **152**, 36-51 (2005). https://doi.org/10.1016/j.jsb.2005.07.007

57 Heymann, J. B. & Belnap, D. M. Bsoft: image processing and molecular modeling for electron microscopy. *J Struct Biol* **157**, 3-18 (2007). https://doi.org/10.1016/j.jsb.2006.06.006

58 Grant, T., Rohou, A. & Grigorieff, N. cisTEM, user-friendly software for single-particle image processing. *Elife* **7** (2018). https://doi.org/10.7554/eLife.35383

59 Rohou, A. & Grigorieff, N. CTFFIND4: Fast and accurate defocus estimation from electron micrographs. *J Struct Biol* **192**, 216-221 (2015). https://doi.org/https://doi.org/10.1016/j.jsb.2015.08.008

60 Punjani, A., Rubinstein, J. L., Fleet, D. J. & Brubaker, M. A. cryoSPARC: algorithms for rapid unsupervised cryo-EM structure determination. *Nature Methods* **14**, 290-296 (2017). https://doi.org/10.1038/nmeth.4169

61 Zheng, S. Q. *et al.* MotionCor2: anisotropic correction of beam-induced motion for improved cryo-electron microscopy. *Nature Methods* **14**, 331-332 (2017). https://doi.org/10.1038/nmeth.4193

62 Punjani, A., Zhang, H. & Fleet, D. J. Non-uniform refinement: adaptive regularization improves single-particle cryo-EM reconstruction. *Nature Methods* **17**, 1214-1221 (2020). https://doi.org/10.1038/s41592-020-00990-8

63 Campbell, M. G. *et al.* Movies of ice-embedded particles enhance resolution in electron cryo-microscopy. *Structure* **20**, 1823-1828 (2012). https://doi.org/10.1016/j.str.2012.08.026

64 Pettersen, E. F. *et al.* UCSF ChimeraX: Structure visualization for researchers, educators, and developers. *Protein Sci* **30**, 70-82 (2021). https://doi.org/10.1002/pro.3943

65 Emsley, P., Lohkamp, B., Scott, W. G. & Cowtan, K. Features and development of Coot. *Acta Crystallogr D Biol Crystallogr* **66**, 486-501 (2010). https://doi.org/10.1107/s0907444910007493

66 Moriarty, N. W., Grosse-Kunstleve, R. W. & Adams, P. D. electronic Ligand Builder and Optimization Workbench (eLBOW): a tool for ligand coordinate and restraint generation. *Acta Crystallogr D Biol Crystallogr* **65**, 1074-1080 (2009). https://doi.org/10.1107/s0907444909029436

67 Liebschner, D. *et al.* Macromolecular structure determination using X-rays, neutrons and electrons: recent developments in Phenix. *Acta Crystallogr D Struct Biol* **75**, 861-877 (2019). https://doi.org/10.1107/s2059798319011471

68 Williams, C. J. *et al.* MolProbity: More and better reference data for improved all-atom structure validation. *Protein Science* **27**, 293-315 (2018). https://doi.org/https://doi.org/10.1002/pro.3330

69 Iudin, A. *et al.* EMPIAR: the Electron Microscopy Public Image Archive. *Nucleic Acids Research* **51**, D1503-D1511 (2022). https://doi.org/10.1093/nar/gkac1062

70 Sorensen, M. *et al.* Rapid microbial identification and colistin resistance detection via MALDI-TOF MS using a novel on-target extraction of membrane lipids. *Sci Rep* **10**, 21536 (2020). https://doi.org/10.1038/s41598-020-78401-3

71 Wu, E. L. *et al.* CHARMM-GUI Membrane Builder toward realistic biological membrane simulations. *J Comput Chem* **35**, 1997-2004 (2014). https://doi.org/10.1002/jcc.23702

72 Kalé, L. *et al.* NAMD2: Greater Scalability for Parallel Molecular Dynamics. *Journal of Computational Physics* **151**, 283-312 (1999). https://doi.org/https://doi.org/10.1006/jcph.1999.6201

73 MacKerell, A. D., Jr., Feig, M. & Brooks, C. L., 3rd. Improved treatment of the protein backbone in empirical force fields. *Journal of the American Chemical Society* **126**, 698-699 (2004). https://doi.org/10.1021/ja036959e

74 Darden, T., York, D. & Pedersen, L. Particle Mesh Ewald - An N.Log(N) Method for Ewald Sums in Large Systems. *Journal of Chemical Physics* **98**, 10089-10092 (1993).

75 Humphrey, W., Dalke, A. & Schulten, K. VMD: visual molecular dynamics. *J.Mol.Graph.* **14**, 33-38 (1996).

76 Abraham, M. J. M., T.; Schulz, R.; Páll, S.; Smith, J.C.; Hess, B.; Lindahl, E. GROMACS: High performance molecular simulations through multi-level parallelism from laptops to supercomputers. *SoftwareX* **1-2**, 19-25 (2015).

77 Vanegas, J. M., Torres-Sanchez, A. & Arroyo, M. Importance of Force Decomposition for Local Stress Calculations in Biomembrane Molecular Simulations. *J Chem Theory Comput* **10**, 691-702 (2014). https://doi.org/10.1021/ct4008926

78 Torres-Sanchez, A., Vanegas, J. M. & Arroyo, M. Examining the Mechanical Equilibrium of Microscopic Stresses in Molecular Simulations. *Phys Rev Lett* **114**, 258102 (2015). https://doi.org/10.1103/PhysRevLett.114.258102

79 Vanegas, J. M. & Arroyo, M. Force transduction and lipid binding in MscL: a continuum-molecular approach. *PLoS One* **9**, e113947 (2014). https://doi.org/10.1371/journal.pone.0113947

80 Ayachit, U. B., A.; Geveci, B.; O'Leary, P.; Moreland, K.; Fabian, N; Mauldin, J. in *2015ACM. ISBN978-1-4503-4003-8/15/11.* 25-29.

81 Martinac, B., Buechner, M., Delcour, A. H., Adler, J. & Kung, C. Pressure-sensitive ion channel in *Escherichia coli*. *PNAS* **84**, 2297-2301 (1987).

82 Li, Y., Moe, P. C., Chandrasekaran, S., Booth, I. R. & Blount, P. Ionic regulation of MscK, a mechanosensitive channel from *Escherichia coli*. *EMBO J.* **21**, 5323-5330 (2002).

83 Belyy, V., Kamaraju, K., Akitake, B., Anishkin, A. & Sukharev, S. Adaptive behavior of bacterial mechanosensitive channels is coupled to membrane mechanics. *J Gen Physiol* **135**, 641-652 (2010).

892 **Acknowledgements**
893 We thank Patrick O'Reilly for composing and illustrating a detailed analysis of membrane protein
894 extraction for Extended Data Fig. 2. We are grateful to Joshua Zimmerberg and Jennifer Peterson for
895 access to the Tecnai T20 electron microscope, AJ Morton, Zabrina Lang, and Rick K. Huang for the
896 support on the G1 Krios, and Wyatt Peele, Kedar Sharma, and Mario Borgnia for the support on the G4
897 Krios. We thank Samantha Miller for providing the MJF465 strain, Paul Blount for providing the PB113
898 strain, Manuela Zoonens for providing the CyclAPol C_8-C_0-50 polymer, Jake Rosetto for assistance with
899 spheroplasting and patch-clamp, Gerald Kidd for assistance in membrane isolation, and Alex Sodt and
900 Louis Tung Faat Lai for valuable discussions. The research was supported by the Division of Intramural
901 Research of the *Eunice Kennedy Shriver* National Institute of Child Health and Human Development,
902 NIH (grant NICHD intramural projects Z1A HD008998 to DM). This work was supported by NIH R01-
903 AI135015 to SS. JMV acknowledges the support of the National Science Foundation through Grant No.
904 CHE-1944892/2326678. This material is based upon work supported by the National Science Foundation
905 Graduate Research Fellowship Program to EM under Grant No. DGE 1840340. Any opinions, findings,
906 and conclusions or recommendations expressed in this material are those of the author(s) and do not
907 necessarily reflect the views of the National Science Foundation. This work utilized the computational
908 resources of the NIH HPC Biowulf cluster (http://hpc.nih.gov). Molecular graphics and analyses
909 performed with UCSF ChimeraX, developed by the Resource for Biocomputing, Visualization, and
910 Informatics at UCSF, with support from NIH R01-GM129325 and the Office of Cyber Infrastructure and
911 Computational Biology, NIAID.
912

913 **Author Contributions**
914 EM: membrane isolation, protein purification, biochemistry (SDS, Western, BN), negative stain
915 microscopy and data collection, cryo-EM grid preparation, cryo-EM data processing, model building and
916 refinement, mutagenesis, patch-clamp, data interpretation, figure making, writing, funding
917 MB: membrane isolation, patch-clamp, figure making, writing
918 FZ: biochemistry advice, cryo-EM grid screening, Krios data collection
919 HY: lipid mass spec, data interpretation, writing
920 AA: molecular dynamics simulations, data interpretation, writing
921 RE: lipid mass spec, data interpretation, writing
922 JMV: molecular dynamics simulations, stress and traction force computation, data interpretation, figure
923 making, writing
924 SS: membrane isolation, sample preparation for mass spec, data interpretation, writing, supervision and
925 training, funding

DM: model building, data interpretation, writing, supervision and training, funding

Competing Interest Declaration

The authors declare no competing interests.

Additional Information

Supplementary Information is available for this paper.

Correspondence and requests for materials should be addressed to Sergei Sukharev (sukharev@umd.edu) and/or Doreen Matthies (Doreen.Matthies@nih.gov).

Data Availability

The data that support this study are available from the corresponding authors upon request. Cryo-EM maps have been deposited in the Electron Microscopy Data Bank (EMDB) under accession codes EMD-71088 (C7 MscS in Glyco-DIBMA) and EMD-71089 (C1 MscS in Glyco-DIBMA). Raw movies will be uploaded to the Electron Microscopy Public Image Archive (EMPIAR). The atomic coordinates have been deposited in the Protein Data Bank (PDB) under accession codes 9P0N (C7 MscS in Glyco-DIBMA) and 9P0O (C1 MscS in Glyco-DIBMA). The source data for Extended Data Fig. 3 and 4 are provided in the Source Data file with this paper.

Code Availability

The scripts used in this study are available from the corresponding authors upon request.